Available online at www.sciencedirect.com

ScienceDirect

Acta Materialia 86 (2015) 279–285

Acta MATERIALIA

www.elsevier.com/locate/actamat

Influence of film thickness and composition on the martensitic transformation in epitaxial Ni–Mn–Sn thin films

N. Teichert,[a,*] A. Auge,[a] E. Yüzüak,[b,c] I. Dincer,[b] Y. Elerman,[b] B. Krumme,[d] H. Wende,[d] O. Yildirim,[e,f] K. Potzger[e] and A. Hütten[a]

[a]*Center for Spinelectronic Materials and Devices, Physics Department, Bielefeld University, 33615 Bielefeld, Germany*
[b]*Department of Engineering Physics, Faculty of Engineering, Ankara University, 06100 Besevler, Ankara, Turkey*
[c]*Department of Nanotechnology Engineering, Faculty of Engineering, Recep Tayyip Erdogan University, 53100 Rize, Turkey*
[d]*Faculty of Physics and Center for Nanointegration Duisburg-Essen (CeNIDE), University of Duisburg-Essen, 47048 Duisburg, Germany*
[e]*Institute of Ion Beam Physics and Materials Research, Helmholtz-Zentrum Dresden-Rossendorf, PO Box 510119, 01314 Dresden, Germany*
[f]*Institute for Physics of Solids, Technical University Dresden, Zellescher Weg 16, 01069 Dresden, Germany*

Received 1 June 2014; revised 9 December 2014; accepted 9 December 2014
Available online 12 January 2015

Abstract—Two series of epitaxial Ni–Mn–Sn thin films of different thickness are investigated for the thickness and composition dependence of the martensitic transformation. Thin films ranging in thickness from 20 to 200 nm (series A) and 10 to 100 nm (series B) were prepared by magnetron co-sputtering and deposited on heated MgO(001) substrates. The structural characterization was done by temperature-dependent X-ray diffraction measurements. Magnetization and resistivity measurements were performed to investigate the transformation characteristics. We find a strong influence of the film thickness on the relative amount of material undergoing the martensitic transformation, the temperature range of the transformation, and the transformation temperatures. The main contribution originates from the rigid substrate which delays the transformation of the Ni–Mn–Sn near the interface and even leads to a layer of residual austenite at low temperatures. Another issue are size effects which presumably broaden the martensitic transformation and decrease the transformation temperatures. By variation of the thin film composition we find changes of the substrate influence due to a different mismatch between the lattice of MgO and austenite. A better phase compatibility between martensite and austenite, denoted by λ_2, not only results in a smaller hysteresis but is also beneficial for the transformation of material close to the substrate.

Keywords: Martensitic transformation; Magnetic thin films; Ferromagnetic shape memory alloys; Magnetocaloric effect

1. Introduction

Ferromagnetic shape memory alloys (FSMAs) are materials in which the martensitic transformation can be controlled by temperature, pressure or a magnetic field [1,2]. These properties make FSMAs promising for use as actuators [3] and in magnetocaloric devices [4]. The most widely studied FSMA is the Heusler compound Ni_2MnGa which shows a martensitic transformation around the stoichiometric composition [5]. Other Heusler alloys of the form Ni–Mn–X (X = In, Sn, Sb) also show a martensitic transformation in a certain off-stoichiometric composition range and have been extensively studied for the past decade [6]. Thin-film FSMAs can act as central elements in future miniaturized cooling devices or micro- and nanoelectromechanical systems. Therefore, a detailed knowledge about thin-film FSMAs is needed. From theoretical and experimental studies it is known that grain size and film thickness have a strong influence on the martensitic transformation characteristics in small-grained material and thin films [7,8]. A change in the transformation temperatures as well as a broadening of temperature range of the transformation was noted. The major influences were found to be substrate constraints [9] and size effects [8].

When working with thin films the choice of an appropriate substrate material is crucial because this has a major influence on the texture and crystalline quality. Usually epitaxial growth is preferred to fix the crystallographic orientation of the crystallites. For Ni–Mn-based Heusler alloy thin films, MgO(001) substrates are mainly used to obtain epitaxial growth. The reduced symmetry in epitaxial films leads preferentially to certain twin boundary and habit plane orientations [10]. In addition, the presence of the substrate can lead to stress-induced martensite or a preference for austenite at the interface [11,12].

Few experimental studies on the thickness dependence of the transformation properties of Ni–Mn-based shape memory Heusler alloys have been reported in the literature. Vishnoi et al. studied non-epitaxial Ni–Mn–Sn thin films on

* Corresponding author; e-mail: nteichert@physik.uni-bielefeld.de

http://dx.doi.org/10.1016/j.actamat.2014.12.019
1359-6462/

Si substrates in the thickness range between 120 nm and 2.5 μm and found a suppression of the martensitic transformation below 410 nm [13]. Recently Ranzieri et al. investigated epitaxial Ni–Mn–Ga films between 10 and 100 nm thick which show a martensitic transformation above 40 nm [14]. For our study we chose Ni–Mn–Sn as a material system because it is easy to adjust the composition by magnetron co-sputtering from elemental targets; furthermore, the lattice mismatch between MgO(1 1 0) and Ni–Mn–Sn(1 0 0) is typically below 1% which leads to very low substrate-induced strain.

In an earlier study we investigated the film thickness dependence of Ni–Mn–Sn thin films 10–100 nm thick and found a martensitic transformation down to 10 nm film thickness [15]. In the present paper, a second film thickness series with slightly different composition and thicknesses between 20 and 200 nm is introduced. The results of both series are presented and compared in detail in order to find the origins for the thickness dependence of the martensitic transformation. Studies about the magnetocaloric properties and exchange bias of the 200 nm film of this series are published elsewhere [16,17].

The purpose of this paper is to expand the knowledge of the martensitic transformation in thin films and to examine the applicability of Ni–Mn–Sn as a suitable material for future thin-film applications.

2. Experimental

The Ni–Mn–Sn thin films were grown on single-crystal MgO(001) substrates using an ultrahigh-vacuum magnetron co-sputtering system. More details of the sample fabrication are given in Ref. [15].

Two sample series with varying thicknesses were prepared: series A with composition $Ni_{51.6}Mn_{32.9}Sn_{15.5}$ and film thicknesses 20, 35, 50, 100 and 200 nm; and series B with the composition $Ni_{51.6}Mn_{34.9}Sn_{13.5}$ and film thicknesses 10, 20, 35, 50, 75 and 100 nm. The error in the composition is estimated to ±2 at.% while the composition difference between series A and B is more exact.

The film composition and thickness were verified by X-ray fluorescence spectroscopy and X-ray reflectometry (XRR), respectively. Structural analysis was done by temperature-dependent X-ray diffraction (XRD) measurements in the temperature range between 243 and 400 K. The magnetic properties were measured in a superconducting quantum interference device magnetometer (Quantum Design MPMS XL) between 10 and 330 K. Field-cooled (FC) and field-heated (FH) magnetization measurements were performed. An in-plane magnetic field of 5 mT for series A and 15 mT for series B was applied during the measurements to observe the magnetic properties of these films under a weak magnetic field. For the investigation of the electric transport properties, a standard four-probe measurement setup with a temperature range from 20 to 370 K was used in a zero magnetic field.

3. Results

3.1. Structural characterization

From the obtained film compositions, the valence electron concentrations e/a are calculated to be 8.083 and 8.143 for series A and B, respectively. The expected martensite start temperatures for the bulk Ni–Mn–Sn are approximately 260 and 360 K, respectively [2].

The structural characterization by XRD in the austenite phase was performed using the Bragg–Brentano configuration at room temperature for series A and at 375 K for series B to obtain a fully austenitic state. The XRD patterns of series A are shown in Fig. 1a. The patterns of series B are similar and are not shown here. As expected, the $(0\,0\,2)_A$ and $(0\,0\,4)_A$ reflections of the austenite phase are visible. The epitaxial relation between film and substrate is MgO(0 0 1)[1 1 0]||Ni–Mn–Sn(0 0 1)[1 0 0]. The Ni–Mn–Sn$(1\,1\,1)_A$ reflection has been measured under 54.7° tilt of the specimen with the MgO(1 0 0) direction parallel to the primary beam in a four-circle diffractometer. The existence of the Ni–Mn–Sn $(1\,1\,1)_A$ reflection (shown in Ref. [15]) indicates crystallization in the $L2_1$ structure. The very small peak at 49.8° in Fig. 1a probably belongs to a binary Ni_3Mn precipitate. It is present in both series but has presumably no significant effect on the martensitic transformation of Ni–Mn–Sn [15].

In Fig. 1b, the film thickness dependence of the out-of-plane lattice constant of the austenite phase is depicted. One can clearly see a relaxation of the lattice constant to greater thicknesses for both series. The lattice mismatch between austenite and MgO ($\sqrt{2}\,a_{MgO} = 5.957$ Å) is 0.5% for series A and 0.2% for series B for the 100 nm films of each series.

The rocking curve integral widths, depicted in Fig. 1c, decrease with increasing film thickness for both series. The 10 nm film of series B is an exception and shows the lowest rocking curve width within series B. The rocking curve width is due to the density of mismatch dislocations. These form above a critical film thickness to relax the strain

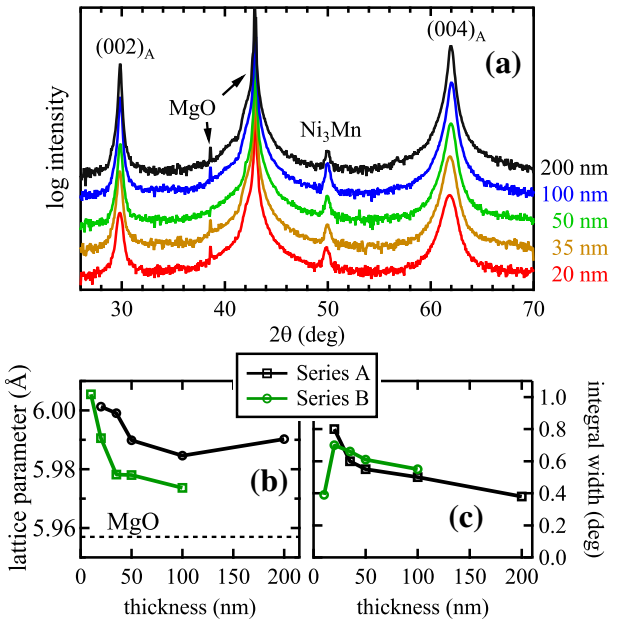

Fig. 1. XRD of the austenite phase. (a) XRD patterns of the austenite phase of series A. (b) The out-of-plane lattice parameter of austenite. (c) The integral width of the $(0\,0\,4)_A$ rocking curve vs. the film thickness for series A (black) and series B (green). The dashed line in (b) marks the lattice parameter of MgO. (For interpretation of the references to color in this figure legend, the reader is referred to the web version of this article.)

induced by the lattice mismatch between film and substrate [18].

The 10 nm film is highly strained, which can also be seen in Fig. 1b, and thus a low density of misfit dislocations is presumed. Hence, the critical thickness for the formation of misfit dislocations is between 10 and 20 nm for series B. This is in accordance with the strong relaxation of the lattice parameter at that thickness (cf. Fig. 1b).

The difference in the rocking curve width between series A and B for the 20 nm films can be explained by the lower lattice mismatch of series B. With further thickness increase, the influence of the lattice relaxation close to the substrate is reduced and hence lower rocking curve widths are obtained.

The average surface roughness of the Ni–Mn–Sn films, determined by XRR, is less than 0.5 nm.

The martensitic lattice structure was analyzed for the 100 nm films of each series. A detailed structural analysis of the martensite phase of series B is given in Ref. [15], where the structure was identified as orthorhombic 10M and 4O. For series A, the results of the structural analysis by XRD are depicted in Fig. 2. In Fig. 2a it can be seen that for 213 K the film is in the martensitic state and the three peaks related to the orthorhombic martensite are present. With increasing temperature, the orthorhombic peaks decrease, and above 273 K only the sharp $(004)_A$ peak of the cubic austenite is present. The $(004)_A/(040)_M$ was measured with sample surface parallel to the direct beam. The $(400)_M$ and $(004)_M$ peaks were measured under 1.6° and 2.5° sample tilt around $[010]_A$, respectively. From Fig. 2b it can be seen that the martensitic peaks start to decrease around 230 K. Thus, this is the austenite start temperature A_s. At 275 K the martensite peaks are nearly zero and the austenite finish temperature A_f is reached. A complete determination of the transformation temperatures is performed by resistivity measurements in Section 3.3.

The temperature dependence of the lattice constants is shown in Fig. 2c. The austenite lattice constant increases linearly above A_f due to thermal expansion. Between A_s and A_f the peak related to the given lattice constant is a superposition of $(004)_A$ and $(040)_M$ and thus the lattice constant deviates from the linear behavior. The martensite lattice constants $(400)_M$ and $(004)_M$ also increase linearly with increasing temperature.

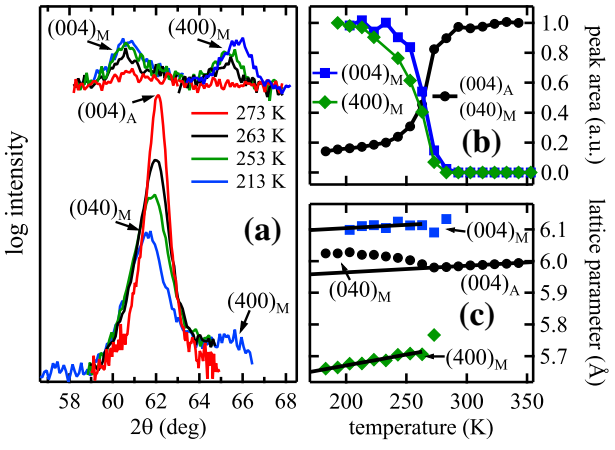

Fig. 2. Temperature-dependent XRD for the 100 nm film of series A. (a) θ–2θ scans of $(004)_A$, and $\{400\}_M$ reflections for different temperatures during the heating cycle. The upper curves showing $(004)_M$ and $(400)_M$ were measured under 2.5° and 1.9° tilt of the sample around $[010]_A$, respectively, and are shifted vertically for reasons of clarity. (b) The normalized integrated intensities of the peaks. (c) The temperature dependence of the lattice constants of the cubic austenite and orthorhombic martensite.

3.2. Magnetism

The results of the magnetization measurements are depicted in Fig. 3. All films are ferromagnetic below the Curie temperature of the austenite T_C^A which is determined by differentiation of the magnetization. The measurements reveal significant differences between series A and B. For the films of series A, the magnetization increases up to 1.1 μ_B/f.u. below T_C^A. The FC and FH curves do not retrace and form a thermal hysteresis, which is attributed to the martensitic transformation. In the FC measurement below the onset of the transformation, the magnetization drops because the magnetization of martensite is lower than of austenite. With decreasing film thickness, the transformation starts at lower temperatures and a broadening of the thermal hysteresis can be seen. In the magnetic measurements of series B, the onset of the martensitic transformation is not visible because it lies above T_C^A. For film thicknesses above 35 nm, the martensite Curie temperature T_C^M is visible. With decreasing film thickness, the gain of magnetization below T_C^A increases. This is due to a shift

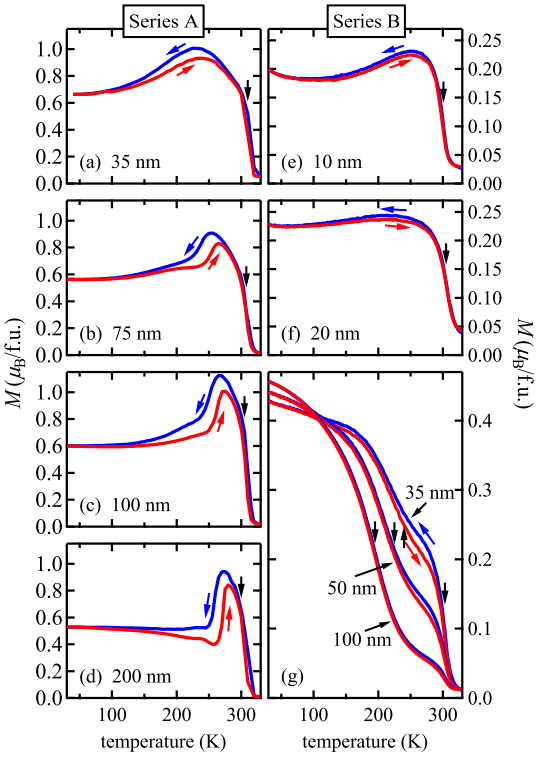

Fig. 3. $M(T)$ at low external field. The $M(T)$ curves of series A are depicted in (a)–(d) for series A and in (e)–(g) for series B. The vertical black arrows indicate the Curie temperatures. The blue arrow indicates field cooling and the red arrow field heating. Series A was measured with an applied field of 5 mT and series B with 15 mT. (For interpretation of the references to color in this figure legend, the reader is referred to the web version of this article.)

of the transformation to lower temperatures and thus a higher fraction of austenite at T_C^A.

The Curie temperatures are listed in Table 1. All measured T_C^A are in reasonable agreement with the values given in the literature. The influence of the film thickness on the austenite Curie temperature is small for both series. T_C^M of the 100 nm film of series B agrees well with the bulk value, but increases with decreasing film thickness. A possible reason for this is the increasing amount of austenite at the respective temperatures with decreasing film thickness. The vicinity of the ferromagnetic austenite strengthens the ferromagnetism in the martensite and shifts T_C^M to higher temperatures.

3.3. Electrical transport

Since the Curie temperatures of series B lie within the range of the martensitic transformation, temperature-dependent resistivity measurements are more suitable for the characterization of the martensitic transformation than magnetic measurements. The results are presented as relative resistivity change

$$\delta\rho(T) = \frac{\rho(T) - \rho_{min}}{\rho_{min}} \quad (1)$$

in Fig. 4, where $\rho(T)$ is the resistivity and ρ_{min} denotes the minimum resistivity. All measurements show an increase in the resistivity at lower temperatures accompanied by a thermal hysteresis between cooling and heating, indicating the occurence of a martensitic transformation. The resistivity of the martensite phase is higher than that of the austenite phase due to a variation of the density of states near the Fermi surface and a higher scattering from defects [19].

Some general trends are observed for both series: with decreasing film thickness, the slope in the transformation region becomes shallower and the temperature range of the transformation broadens. Also, the maximum resistivity change decreases with decreasing film thickness. Furthermore, in all measurements the transformation region shows two regimes: an almost linear increase with decreasing temperature is followed by a reduction of the slope over a wide temperature range.

Comparing $\rho(T)$ and $M(T)$, or Figs. 3 and 4, reveals that the thermal hysteresis extends over a similar temperature range for series A, and the 10 nm film of series B. For the thicker films of series B, the transformation starts above the Curie temperature, and thus the transformation is only partially visible in the magnetization results.

In the following, the characteristics of the martensitic transformation are discussed on the basis of the resistivity measurements. The transformation temperatures are extracted from the intersections of extrapolations from linear regions, as indicated in Fig. 4 [20,21]. M_s (M_f) and A_s (A_f) are the martensite and austenite start (finish) temperatures, respectively. $\Delta\tau = ((M_s + A_f) - (M_f + A_s))/2$ defines the temperature range of the linear transformation region. The width of the thermal hysteresis is defined as $\Delta T_h = ((A_f - M_s) + (A_s - M_f))/2$. The characteristic temperatures and hysteresis widths are given in Table 2. M_s of the thickest films of both series are in good agreement with literature values for bulk (see Section 3.1).

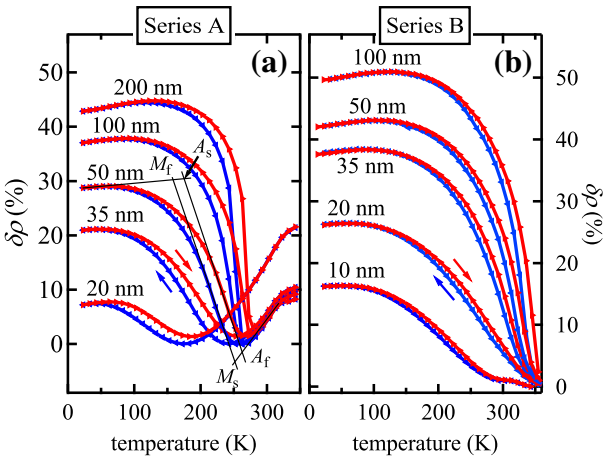

Fig. 4. Electrical transport. The normalized resistivity vs. temperature for each film is shown in (a) for series A and in (b) for series B. The red and blue arrows indicate the direction of temperature change. The method of determining the transition temperatures is indicated by black lines. (For interpretation of the references to color in this figure legend, the reader is referred to the web version of this article.)

Fig. 5 gives an overview for the thickness dependence of the martensitic transformation and Curie temperatures. As also shown in Table 2, A_s and M_f show the strongest dependency on the film thickness. They reduce by 165 K between 200 and 20 nm in series A and by 177 K between 100 and 10 nm in series B. The impact of the film thickness on M_s and A_f is much less. They drop by only about 60 K within series A and by 68 K within series B. The transformation range $\Delta\tau$ increases from 25 K for 200 nm to 134 K for 20 nm in series A and from 58 K for 100 nm to 165 K for 10 nm in series B.

The resistivity change due to the martensitic transformation differs between series A and B. The total resistivity change $\delta\rho_{max}$ is about 50% for series B and only 38% for series A for 100 nm film thickness. A possible explanation for this difference and the reduction of $\delta\rho_{max}$ with decreasing thickness is given by the following model. An austenite layer which cannot transform due to constraints remains close to the MgO substrate. This austenite layer is assumed to be independent of the film thickness and thus loses influence in thicker films. Therefore, at low temperatures a film

Table 1. The Curie temperatures of the austenite T_C^A and martensite T_C^M of both thin film series as well as reference values for bulk from the literature.

h (nm)	10	20	35	50	75	100	200	Bulk[a]
Series A								
T_C^A (K)			310		308	305	300	317
Series B								
T_C^A (K)	301	305	305	302		301		≈312
T_C^M (K)			240	225		195		203

[a] Ref. [2].

Table 2. The transformation temperatures and the width of the thermal hysteresis ΔT_h for each film. The transition temperatures are determined from resistivity measurements as indicated in Fig. 4.

h (nm)	M_s (K)	A_f (K)	M_f (K)	A_s (K)	$\Delta\tau$	ΔT_h (K)
Series A						
20	207	215	64	90	134	17
35	244	254	107	126	134	15.5
50	252	263	159	176	90	14
75	255	269	197	216	56	16.5
100	259	274	212	228	47	15.5
200	263	275	233	255	25	17
Series B						
10	281	290	116	125	165	9
20	331	339	151	164	178	10.5
35	330	336	218	232	108	10
50	335	344	254	263	82	9
100	347	358	288	302	58	12.5

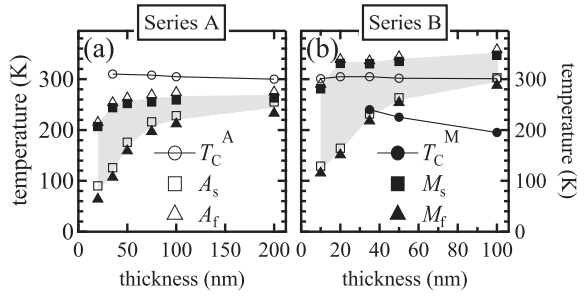

Fig. 5. Phase diagrams of (a) series A and (b) series B. The light gray area shows the temperature range of the martensitic transformation.

can be treated as a parallel resistor with a martensite layer of high resistivity and an austenite layer of low resistivity. The relative resistivity change towards the austenite resistivity at temperature T_a below M_f is then:

$$\Delta\rho(h,T_a)=\frac{\rho(T_a)}{\rho_A(T_a)}-1=\frac{h}{h_A+\frac{\rho_A(T_a)}{\rho_M(T_a)}(h-h_A)}-1 \qquad (2)$$

where h is the film thickness, h_A is the thickness of the austenite layer, and ρ_M and ρ_A are the low-temperature resistivities of austenite and martensite, respectively. ρ_A at low temperatures is taken from resistivity data of a 20 nm film with slightly different composition, where no martensitic transformation is visible. The temperature point $T_a = 53$ K is chosen to compare the relative difference in resistivity between fully austenitic and transformed thin film. The relative resistivity change towards ρ_A is depicted in Fig. 6a as an exemplar for series A and the extracted data $(\rho(T_a)/\rho_A(T_a)-1)$ are depicted in Fig. 6b along with the fit using Eq. (2). The fit parameters are h_A and $\rho_A(T_a)/\rho_M(T_a)$. The fit is in good agreement to the data (cf. Fig. 6b) and results in austenite layer thicknesses $h_A^A = 8.4$ nm and $h_A^B = 2.5$ nm for series A and B, respectively. From the latter fit parameter, the relative resistivity change between austenite at high temperature and martensite at low temperature is calculated since this allows comparison with other published works. The temperatures 343 and 53 K are chosen for this purpose. This quantity $\rho_M(53\,\mathrm{K})/\rho_A(343\,\mathrm{K})$ is 1.38 for series A and 1.51 for series B. In Table 3, the results from this work and some published results for bulk material with similar compositions are summarized. The applied

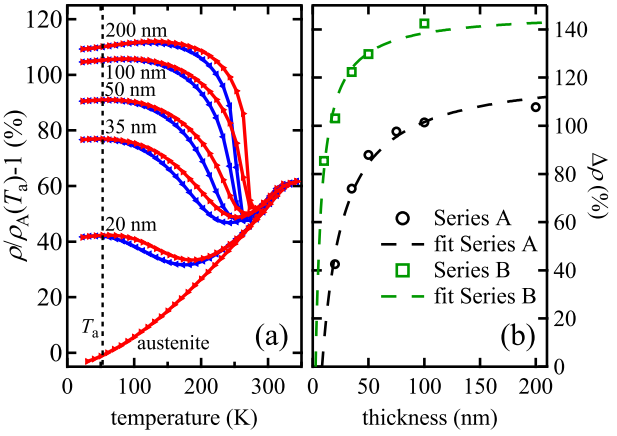

Fig. 6. Analysis of the resistivity change. The resistivities of series A and of an austenitic 20 nm Ni–Mn–Sn film is shown in (a). The curves are normalized to a common value at 343 K. The dashed vertical line indicates $T_a = 53$ K. In (b) the resistivity change at T_a is depicted by the black round (green square) markers for series A (series B). The black (green) dashed line depicts the fit using Eq. (2) for series A (series B). (For interpretation of the references to color in this figure legend, the reader is referred to the web version of this article.)

Table 3. The film thickness of the residual austenite h_A and the ratio $\rho_M(53\,\mathrm{K})/\rho_A(343\,\mathrm{K})$ are obtained from the parallel resistor model (cf. Eq. (2) and Fig. 6). Values from the literature for bulk material with similar composition and e/a ratio are given for comparison.

Composition	e/a	h_A	$\frac{\rho_M(53\,\mathrm{K})}{\rho_A(343\,\mathrm{K})}$
Series A			
$Ni_{51.6}Mn_{32.9}Sn_{15.5}$	8.083	8.4 nm	1.38
$Ni_{50}Mn_{36}Sn_{14}$ [a]	8.08		1.31
$Ni_{50}Mn_{36}Sn_{14}$ [b]	8.08		1.48
Series B			
$Ni_{51.6}Mn_{34.9}Sn_{13.5}$	8.143	2.5 nm	1.51
$Ni_{50}Mn_{38}Sn_{12}$ [a]	8.14		1.44

[a] Ref. [22].
[b] Ref. [23].

model allows only for an assessment of the amount of residual austenite because some influences could not be taken into account. The austenite resistivity at low temperature

is estimated using a Ni–Mn–Sn film of different composition to remain austenitic at low temperature and the resistivity curves have been normalized to have a common value at 343 K. In addition, twin coarsening with increasing film thickness as seen by Kaufmann et al. in Ni–Mn–Ga films might lead to a film thickness dependence of the martensite resistivity which was not taken into account [10]. However, despite its simplicity, the model is in good agreement with the measurement and the obtained results are consistent with the literature (Table 3).

4. Discussion

In the following, the characteristics of the martensitic transformations in Ni–Mn–Sn thin films are discussed: (i) a higher amount of residual austenite in series A, (ii) a broadened transformation range below the determined transformation temperatures M_f and A_s, (iii) a shift of the transformation temperatures and broadening of the transformation range $\Delta\tau$ with decreasing film thickness, and (iv) a smaller thermal hysteresis ΔT_h in series B. Finally this work is compared to results from other publications.

(i) From the resistivity measurements it was concluded that series A shows more residual austenite than series B. The region of residual austenite is probably at the interface with the substrate. The vicinity of the rigid MgO prevents the transformation of the Ni–Mn–Sn.

The lattice mismatch of series A is higher than for series B; this leads to additional stress upon the austenite at the interface with the substrate. The higher lattice mismatch might also lead to a higher density of misfit dislocations which can prohibit the martensitic transformation. For series A, an influence of the dislocation density is possible but this can be excluded for series B. For series B, the 10 nm film shows the lowest rocking curve width (see Fig. 1c) and the highest out-of-plane lattice constant among the series. Thus, the film thickness is below the critical thickness for the formation of misfit dislocations [18]. On the other hand, the film thickness dependence of $\delta\rho$ of this film fits to the rest of the series, and hence the same amount of residual austenite is expected, leading to the conclusion that the residual austenite is independent of misfit dislocations. For series A, however, the lattice mismatch is higher, which leads to a higher density of misfit dislocations and a lower critical thickness for their formation. The high number of dislocations close to the substrate in series A is reflected in the rocking curve width of the 20 nm film, which is the highest of all studied films. Therefore, for this series an influence of misfit dislocations on the amount of residual austenite seems possible.

Additional to the lattice mismatch, the phase compatibility between martensite and austenite can influence the amount of residual austenite.

According to the theory of nonlinear martensite, which was propounded by James et al. [24,25], the energy barrier resulting from mismatch strain energy between austenite and martensite can be reduced for certain combinations of austenite and martensite lattice parameters. A better phase compatibility leads to a coarser laminate structure of martensite variants which requires less energy for its formation due to fewer twin boundaries being present. Therefore, in the vicinity of the substrate, more material will transform if the phase compatibility is better. The important parameter for this is the second eigenvalue of the Bain transformation matrix, λ_2, where an optimum phase compatibility is reached for $\lambda_2 = 1.0$ [26,27]. With the lattice parameters of austenite and martensite from Table 4, and the transformation matrix for a cubic-to-orthorhombic transition as given in Ref. [26], we find $\lambda_2^A = 1.0092$ and $\lambda_2^B = 1.0055$ for series A and B, respectively. Thus, we find a better phase compatibility for series B which coincides with less residual austenite being present.

(ii) The observed delayed transformation in the temperature range below the linear transformation region fits the concept of an impeded transformation in the vicinity of the substrate. Here, a necessary driving force in the form of additional chemical energy is needed to accomplish the transformation and this is provided by further undercooling.

(iii) From Fig. 5 it can be seen that the lower transformation temperatures (M_f and A_s) are more dependent on the film thickness than the higher ones (M_s and A_f) which leads to an expansion of the transformation range and hence a reduction of the transformation rate.

According to Malygin, these effects are a consequences of the reduced grain size d or film thickness t [8,28]. Those size effects become important if d or t have the same size as the diameter of a new-phase nucleus l or the mean free path of transformation dislocations λ. In this case, constraints arise which hinder the transformation and thus lead to a reduction of the transformation temperatures and possibly to a broadening of the transformation range. Meng et al. found that the grain size of polycrystalline materials influences the martensitic transformation for $d < 100$ nm [29]. A decreasing grain size increases the nucleation barrier and critical size of a nucleus.

Although these considerations qualitatively explain the observations discussed here, the increasing influence of substrate constraints in thinner films can lead to the same effects and could not be distinguished from size effects in this work.

(iv) The last effect to discuss is the behavior of the thermal hysteresis ΔT_h. Cui et al. found a correlation between the phase compatibility, i.e. $\lambda_2 = 1$ and a small ΔT_h, for the Ni–Ti–Cu and Ni–Ti–Pd systems [26]. This was validated and theoretically substantiated by Zhang et al. for other Ni–Ti–X (X = Cu, Pd, Pt, Au) alloys [27]. For Ni–Co–Mn–Sn, which is similar to the Ni-Mn-Sn investigated here, a very small hysteresis of $\Delta T_h = 7$ K combined with $\lambda_2 \approx 1$ was found [30]. In this work, the average thermal hysteresis is $\Delta T_h^A \approx 16$ K and $\Delta T_h^B \approx 10$ K for series A

Table 4. The lattice parameters for martensite and austenite, and λ_2 at temperature T_0 are listed for each series. a_{cub} at the respective temperature was determined using linear extrapolation from the austenite state.

Series	T_0(K)	a_{cub} (Å)	a_{orth} (Å)	b_{orth} (Å)	c_{orth} (Å)	λ_2
A	213	5.967	5.680	6.022	6.102	1.0092
B	293	5.974	5.653	6.007	6.167	1.0055

and B, respectively. Since we find λ_2^B to be closer to 1 than λ_2^A (cf. Table 4), we also observe this correlation.

For comparison of our work with other publications, the papers of Vishnoi et al. [13] and Ranzieri et al. [14] should in particular be considered. Vishnoi et al. investigated polycrystalline $Ni_{50}Mn_{36}Sn_{14}$ films on Si substrate and found a suppression of the martensitic transformation below 410 nm film thickness due to the very small grain sizes. A critical grain size between 9 and 16 nm can be extracted from their work. Our finding of a martensitic transformation even down to 10 nm film thickness is presumably because of a better crystal quality of our films due to epitaxial growth on MgO and low lattice mismatch between film and substrate accompanied by low strain. Ranzieri et al. studied epitaxial $Ni_{52.5}Mn_{19.5}Ga_{28}$ films on MgO substrate and found a critical film thickness of 40 nm. To resolve this, similar arguments as under (i) apply: the lattice mismatch between Ni–Mn–Ga and MgO is, at 2.7%, significantly higher than for Ni–Mn–Sn. Also, as far as it can be extracted from Ranzieri et al. [14], the phase compatibility $\lambda_2^{Ni–Mn–Ga} = 1.04$ is significantly worse than for both Ni–Mn–Sn compositions investigated here. However, differences in the sample preparation and material properties can also lead to a higher critical film thickness.

5. Conclusions

In summary, we have studied epitaxial thin films of $Ni_{51.6}Mn_{32.9}Sn_{15.5}$ (series A) and $Ni_{51.6}Mn_{34.9}Sn_{13.5}$ (series B) on MgO in the thickness range between 10 and 200 nm. The crystalline quality of the films was quantified by XRD in the austenite phase. Temperature-dependent XRD, magnetization and resistivity measurements were performed in order to investigate the characteristics of the martensitic transformation. All investigated films show a martensitic transformation. The resistivity measurements indicate the presence of an amount of residual austenite at low temperatures which is independent of the film thickness. Whereas the thick films (100 and 200 nm) show bulk-like transformation behavior, with decreasing film thickness the transformation becomes less pronounced, the transformation temperatures decrease and the transformation range broadens.

The dominating influences are the rigid substrate, phase compatibility between martensite and austenite, and size effects. The substrate suppresses the transformation at the interface which leads to a layer of residual austenite and a broadened transformation region below M_f. The thickness of this austenite layer decreases with lower lattice misfit between austenite and substrate and with better phase compatibility between martensite and austenite. The width of the thermal hysteresis ΔT_h is also found to decrease with better phase compatibility. Substrate constraints and size effects cause the broadening of the transformation range and a decrease in transformation temperatures with decreasing film thickness.

Based on our findings we recommend epitaxial Ni–Mn–Sn films as a material system for future shape memory or magnetocaloric nanosystems.

Acknowledgment

The authors gratefully acknowledge funding by the DFG through SPP 1599 “Ferroic Cooling”, TÜBİTAK (Project Number 109T582), and DLR (project 01DL12010 “SuBuTu”).

References

[1] A. Sozinov, A.A. Likhachev, N. Lanska, K. Ullakko, Appl. Phys. Lett. 80 (2002) 1746.
[2] A. Planes, L. Mañosa, M. Acet, J. Phys.-Condens. Matter 21 (2009) 233201.
[3] O. Söderberg, Y. Ge, A. Sozinov, S.-P. Hannula, V.K. Lindroos, Smart Mater. Struct. 14 (2005) 223–235.
[4] L. Theil Kuhn, N. Pryds, C.R.H. Bahl, A. Smith, J. Phys. Conf. Ser. 303 (2011) 012082.
[5] K. Ullakko, J.K. Huang, C. Kantner, R.C. O’Handley, Appl. Phys. Lett. 69 (1996) 1966.
[6] Y. Sutou, Y. Imano, N. Koeda, T. Omori, R. Kainuma, K. Ishida, K. Oikawa, Appl. Phys. Lett. 85 (2004) 4358–4360.
[7] D.C. Dunand, P. Müllner, Adv. Mater. 23 (2011) 216.
[8] G.A. Malygin, Tech. Phys. 54 (2009) 1782–1785.
[9] A.L. Roytburd, T.S. Kim, Q. Su, J. Slutsker, M. Wuttig, Acta Mater. 46 (1998) 5095–5107.
[10] S. Kaufmann, R. Niemann, T. Thersleff, U.K. Rößler, O. Heczko, J. Buschbeck, B. Holzapfel, L. Schultz, S. Fähler, New J. Phys. 13 (2011) 053029.
[11] J. Buschbeck, R. Niemann, O. Heczko, M. Thomas, L. Schultz, S. Fähler, Acta Mater. 57 (2009) 2516.
[12] M. Thomas, O. Heczko, J. Buschbeck, U.K. Rößler, J. McCord, N. Scheerbaum, L. Schultz, S. Fähler, New J. Phys. 10 (2008) 023040.
[13] R. Vishnoi, R. Singhal, D. Kaur, J. Nanopart. Res. 13 (2011) 3975–3990.
[14] P. Ranzieri, S. Fabrici, L. Nasi, L. Righi, F. Casoli, V.A. Chernenko, E. Villa, F. Albertini, Acta Mater. 61 (2013) 263.
[15] A. Auge, N. Teichert, M. Meinert, G. Reiss, A. Hütten, E. Yüzüak, I. Dincer, Y. Elerman, I. Ennen, P. Schattschneider, Phys. Rev. B 85 (2012) 214118.
[16] E. Yüzüak, I. Dincer, Y. Elerman, A. Auge, N. Teichert, A. Hütten, Appl. Phys. Lett. 103 (2013) 222403.
[17] A. Behler, N. Teichert, B. Dutta, A. Waske, T. Hickel, A. Auge, A. Hütten, J. Eckert, AIP Adv. 3 (2009) 122112.
[18] M. Ohring, Materials Science of Thin Films, Academic Press, 2001.
[19] O. Heczko, S. Fähler, T.M. Vasilchikova, N. Voloshok, K.V. Klimov, Y.I. Chumlyakov, A.N. Vasiliev, Phys. Rev. B 77 (2008) 174402.
[20] P.J. Shamberger, F.S. Ohuchi, Phys. Rev. B 79 (2009) 14407.
[21] Y. Luo, A. Laptev, M. Fonin, U. Rüdiger, M. Laufenberg, K. Samwer, New J. Phys. 13 (2011) 013042.
[22] S. Chatterjee, S. Majumdar, Mater. Sci. Forum 635 (2010) 97–102.
[23] K. Koyama, H. Okada, K. Watanabe, T. Kanomata, R. Kainuma, W. Ito, K. Oikawa, K. Ishida, Appl. Phys. Lett. 89 (2006) 182510.
[24] J.M. Ball, R.D. James, Arch. Ration. Mech. Anal. 100 (1987) 13.
[25] J.M. Ball, R.D. James, Trans. R. Soc. London A 338 (1992) 389.
[26] J. Cui, Y.S. Chu, O.O. Famodu, Y. Furuya, J. Hattrick-Simpers, R.D. James, A. Ludwig, S. Thienhaus, M. Wuttig, Z. Zhang, I. Takeuchi, Nat. Mater. 5 (2006) 286.
[27] Z. Zhang, R.D. James, S. Müller, Acta Mater. 57 (2009) 4332.
[28] G. Malygin, Phys. Solid State 50 (2008) 1538.
[29] Q. Meng, Y. Rong, T.Y. Hsu, Phys. Rev. B 65 (2002) 174118.
[30] V. Srivastava, X. Chen, R.D. James, Appl. Phys. Lett. 97 (2010) 014101.